

## Magnetic field effects on transport properties of PtSn<sub>4</sub>

Eundeok Mun,<sup>1</sup> Hyunjin Ko,<sup>2</sup> Gordon J. Miller,<sup>2</sup> German D. Samolyuk,<sup>1,\*</sup> Sergey L. Bud'ko,<sup>1</sup> and Paul. C. Canfield<sup>1</sup>

<sup>1</sup>Ames Laboratory US Department of Energy and Department of Physics and Astronomy, Iowa State University, Ames, Iowa 50011, USA

<sup>2</sup>Ames Laboratory US Department of Energy and Department of Chemistry, Iowa State University, Ames, Iowa 50011, USA

(Received 6 October 2011; revised manuscript received 17 January 2012; published 31 January 2012)

The anisotropic physical properties of single crystals of orthorhombic PtSn<sub>4</sub> are reported for magnetic fields up to 140 kOe, applied parallel and perpendicular to the crystallographic **b** axis. The magnetic susceptibility has an approximately temperature-independent behavior and reveals an anisotropy between the **ac** plane and **b** axis. Clear de Haas-van Alphen oscillations in fields as low as 5 kOe and at temperatures as high as 30 K were detected in magnetization isotherms. The thermoelectric power and resistivity of PtSn<sub>4</sub> show the strong temperature and magnetic field dependencies. A change of the thermoelectric power at  $H = 140$  kOe is observed as high as  $\simeq 50$   $\mu$ V/K. Single crystals of PtSn<sub>4</sub> exhibit very large transverse magnetoresistance of  $\simeq 5 \times 10^5\%$  for the **ac** plane and of  $\simeq 1.4 \times 10^5\%$  for the **b** axis resistivity at 1.8 K and 140 kOe, as well as pronounced Shubnikov de Haas oscillations. The magnetoresistance of PtSn<sub>4</sub> appears to obey Kohler's rule in the temperature and field range measured. The Hall resistivity shows a linear temperature dependence at high temperatures followed by a sign reversal around 25 K which is consistent with thermoelectric power measurements. The observed quantum oscillations and band structure calculations indicate that PtSn<sub>4</sub> has three-dimensional Fermi surfaces.

DOI: [10.1103/PhysRevB.85.035135](https://doi.org/10.1103/PhysRevB.85.035135)

PACS number(s): 72.15.Gd, 72.15.Jf, 71.18.+y, 71.20.Lp

### I. INTRODUCTION

In the Pt-Sn binary system, five stoichiometric binary compounds Pt<sub>3</sub>Sn, PtSn, Pt<sub>2</sub>Sn<sub>3</sub>, PtSn<sub>2</sub>, and PtSn<sub>4</sub> have been reported,<sup>1</sup> whereas Pt<sub>3</sub>Sn and PtSn melt congruently, Pt<sub>2</sub>Sn<sub>3</sub>, PtSn<sub>2</sub>, and PtSn<sub>4</sub> decompose peritectically. The Pt-Sn system has been proposed for a wide range of applications such as soldering, dentistry, and jewelry.<sup>2-4</sup> Interestingly, it is observed that the intermetallic phase of PtSn<sub>4</sub> is formed during soldering at the interface of metallization and solder; the dissolution of Pt in SnPb (60/40) solder was found to be linear and the rate of dissolution at 260 °C was 24 nm/min.<sup>2</sup> Only a few studies of physical properties on the Sn-rich side have been performed on polycrystalline samples.<sup>5-7</sup> Although PtSn<sub>4</sub> is a deeply peritectic compound, on the Sn-rich side (95%–99% Sn) it is relatively easy to grow single crystals of PtSn<sub>4</sub> out of a Sn-rich solution.

PtSn<sub>4</sub> compound crystallizes in an orthorhombic structure [PtSn<sub>4</sub>-type, Ccca (No.68),  $z = 4$ ] with lattice constants  $a = 6.418$  Å,  $b = 11.366$  Å, and  $c = 6.384$  Å.<sup>7</sup> This structure can be visualized as consisting of layers which are a stacking of Sn-Pt-Sn layers along the crystallographic **b** axis, as shown in Fig. 1(a). As could be expected from the crystal structure with its pseudotetragonal symmetry,  $a \simeq c \neq b$ , the electrical resistivity and magnetization measurements indicate an axial anisotropy between the **ac** plane and **b** axis with negligible **ac** in-plane anisotropy.

Here we report the physical properties of single crystals of PtSn<sub>4</sub>. The observed electronic and magnetic properties of PtSn<sub>4</sub> are consistent with it being a weakly diamagnetic, intermetallic compound, but with a clear anisotropy. The high quality of the samples has allowed us to experimentally observe the quantum oscillations from the magnetization (de Haas-van Alphen effect, dHvA), resistivity (Shubnikov-de Haas effect, SdH), and thermoelectric power (TEP) measurements. For the magnetic field applied along three different orientations, we found several frequencies for each direction, implying several extremal orbits on the Fermi surface. A large

magnetic field dependence of the resistivity is observed at low temperatures in the highest quality crystals of PtSn<sub>4</sub>, which appears to follow a generalized Kohler's rule with a functional  $\Delta\rho/\rho(0) = F[H/\rho(0)] \simeq H^{1.8}$ .<sup>8</sup> The observed transport properties derived from the Hall coefficient and TEP measurements also show a significant magnetic field dependence.

### II. EXPERIMENTAL METHODS AND STRUCTURE DETERMINATION

Single crystals of PtSn<sub>4</sub> were grown out of a Sn-rich binary melt.<sup>9</sup> The constituent elements, with an initial stoichiometry of Pt<sub>0.04</sub>Sn<sub>0.96</sub>, were placed in an alumina crucible and sealed in a quartz tube under a partial Ar pressure. After the quartz ampoule was heated up to 600 °C, the ampoule was cooled down to 350 °C over 60 h. The crystals grow as large, layered plates shown in Fig. 1(b) and are malleable but also easily cleaved. The crystals are large, typically up to  $\sim 7 \times 7 \times 2$  mm<sup>3</sup>, and an almost 100 % yield of PtSn<sub>4</sub>, based on initial Pt content, can be achieved. The Sn flux was removed using a centrifuge (decanting), and the remaining Sn flux droplets on the surface were removed by etching in concentrated hydrochloric acid (HCl).

Powder x-ray diffraction measurements were taken at room temperature with Cu- $K_{\alpha 1}$  radiation in a Rigaku Miniflex diffractometer. Because of their soft nature, the crystals were ground for x-ray measurements in liquid nitrogen. A typical diffraction pattern of PtSn<sub>4</sub> is shown in Fig. 2. The problem of indexing and determination of the lattice constant in powder diffraction analysis is nontrivial due fundamentally to the significant broadening of peaks, therefore lower angle peaks, below  $2\theta = 60^\circ$ , were selected to determine lattice constants. Most of the detected peaks can be indexed using an orthorhombic (Ccca, No. 68) structure with  $a = 6.42 \pm 0.03$  Å,  $b = 11.42 \pm 0.05$  Å, and  $c = 6.39 \pm 0.03$  Å, which gives a reasonable agreement with single crystal x-ray diffraction

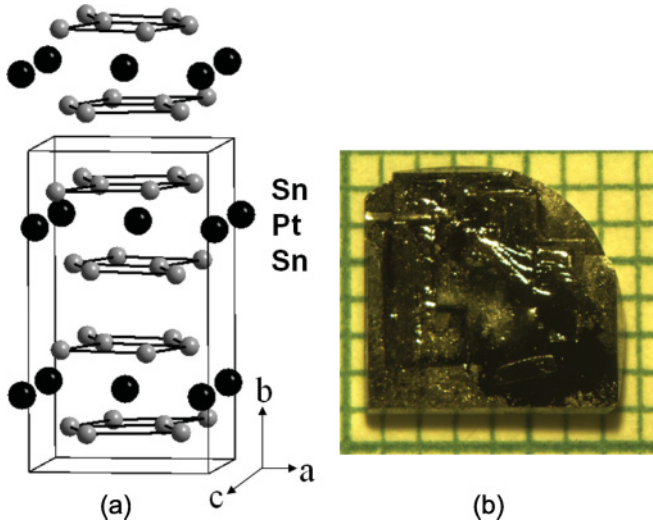


FIG. 1. (Color online) (a) Crystal structure of PtSn<sub>4</sub>, along the **b** axis showing Sn-Pt-Sn layers. (b) Photo of a representative single crystal over a millimeter grid. The **b** axis is perpendicular to the plate.

measurements and is consistent with the earlier report.<sup>7</sup> The observed and calculated patterns are shown in Fig. 2, where we expect that the differences between calculated and observed peak intensities are based on preferred orientation of the powder.

In order to check for atomic positions and site occupancies in PtSn<sub>4</sub> and to confirm space group, multiple single crystals of approximately  $0.1 \times 0.1 \times 0.1$  mm<sup>3</sup> were extracted from several batches for single crystal x-ray diffraction determination of the structure. Room temperature x-ray diffraction data were collected on a STOE-IPDS2-II (Image Plate Diffraction System) single crystal diffractometer with Mo- $K_{\alpha}$  radiation ( $\lambda = 0.71073$  Å; 50 kV and 40 mA) using a PG(002) monochromator. The intensity data sets were used to solve

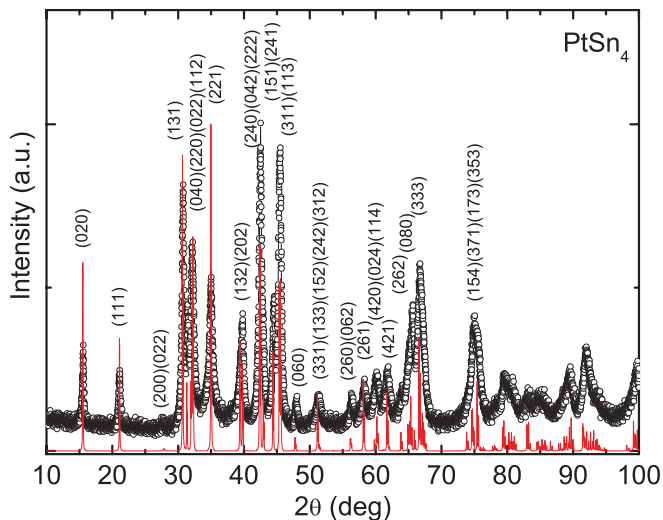


FIG. 2. (Color online) Observed and calculated x-ray powder patterns of PtSn<sub>4</sub>. The open circles represent the observed data points and the solid line represents the calculated pattern. Representative (*hkl*) values are indicated.

and refine the crystal structures with the SHELXTL program suite. The final analysis of the single crystal x-ray diffraction data confirms the space group, lattice parameters, and 100 % site occupancy of the Pt and Sn sites, which were consistent with the earlier study.<sup>7</sup>

The orientation of the crystal was determined by standard Laue techniques, where the **b** axis is perpendicular to the plate and the **a** axis and **c** axis are parallel to the plane as well as the edge facets of the crystals. Unfortunately, due to the small difference between the *a* and *c* lattice constant, and somewhat poor quality of Laue back-scattering data, it was difficult to identify specific edges as **a** or **c**. In this article we will use the orientations **b**,  $\perp \mathbf{bI}$ , and  $\perp \mathbf{bII}$  where  $\perp \mathbf{bI}$  and  $\perp \mathbf{bII}$  are perpendicular, planar directions along the edge facets and are either the **a** axis or **c** axis.

The specific heat was measured by the relaxation technique over the temperature range from 1.8 to 200 K in a Quantum Design (QD) Physical Property Measurement System (PPMS). The magnetization as a function of temperature and field was measured by using a QD Superconducting Quantum Interference Device (SQUID) magnetometer over the temperature range from 1.8 to 300 K and in fields up to 70 kOe. The electrical resistivity was measured using a four-probe, *ac* ( $f = 16$  Hz) technique over temperatures from 1.8 to 305 K and in fields up to 140 kOe in a QD PPMS. For the transverse magnetoresistance (MR) measurements, the magnetic field was applied perpendicular to the current direction,  $\mathbf{H} \perp \mathbf{I}$ , the current was flowing along the *ac* plane of the crystal ( $\mathbf{I} \perp \mathbf{b}$ ) and the magnetic field was applied along either the **b** axis ( $\mathbf{H} \parallel \mathbf{b}$ ) or the *ac* plane ( $\mathbf{H} \perp \mathbf{b}$ ). Hall resistivity measurements were performed in a four-wire geometry, switching the polarity of the magnetic field to remove MR effects due to small misalignments of the voltage wires; the configurations of wires and fields were  $\mathbf{H} \parallel \mathbf{b}$  and  $\mathbf{I} \perp \mathbf{V} \perp \mathbf{b}$ . Thermoelectric power measurements were carried out by a dc, alternating heating (two-heater-two-thermometer) technique<sup>10</sup> over the temperature range from 2 to 300 K and in fields up to 140 kOe.

### III. RESULTS

#### A. Specific heat

The temperature-dependent specific heat,  $C_p$ , data for PtSn<sub>4</sub> in  $H = 0$  and 140 kOe are presented in Fig. 3. The  $C_p$  curves are typical of metallic compounds and do not show any signature of a phase transition. The sample is essentially nonmagnetic and a magnetic field of 140 kOe has essentially no effect on  $C_p(T)$ . The electronic specific heat coefficient  $\gamma$  and the Debye temperature  $\Theta_D$  of PtSn<sub>4</sub> can be obtained by fitting the  $C_p$  data to the relation  $C_p = \gamma T + \beta T^3$  at low temperatures. In zero field,  $\Theta_D$  is estimated to be  $\sim 210$  K and  $\gamma$  is found to be  $\sim 4$  mJ/mol K<sup>2</sup>. The specific heat increases rapidly between 25 and 75 K and on further warming appears to be saturating toward the classical limit of Dulong-Petit law (136.6 J/mol K for PtSn<sub>4</sub>).<sup>11</sup>

#### B. Magnetization

The observed magnetic properties of PtSn<sub>4</sub> are consistent with it being a weakly diamagnetic, intermetallic compound.

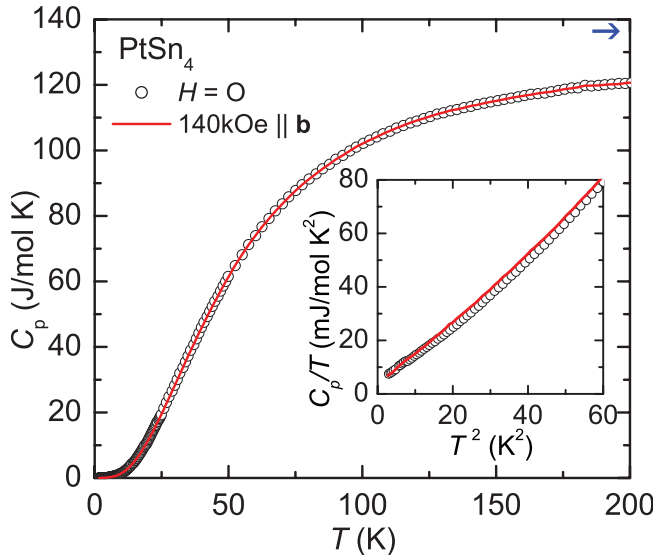


FIG. 3. (Color online) Temperature dependence of the specific heat  $C_p$  of  $\text{PtSn}_4$  in  $H = 0$  (open circle) and 140 kOe (solid line). (Inset)  $C_p/T$  vs  $T^2$  plot. Horizontal arrow in the upper right corner indicates the classical limit of the Dulong-Petit law.

As shown in Fig. 4(a), the magnetization as a function of temperature,  $M(T)/H$ , measured in  $H = 10$  kOe depends only weakly on temperature. The magnetic anisotropy is clearly seen in  $M(T)/H$  between  $\mathbf{H} \parallel \mathbf{b}$  and  $\mathbf{H} \perp \mathbf{b}$ , with essentially no anisotropy being observed within  $\mathbf{ac}$  plane ( $\mathbf{H} \perp \mathbf{bl}$  and  $\mathbf{H} \perp \mathbf{blI}$ ). At low temperatures an oscillatory behavior in  $M(H)$  occurs; dHvA oscillations are shown in Fig. 4(b). This nonlinear low temperature  $M(H)$  is the cause of the variable  $M(T)/H$  shown as the inset to Fig. 4(a).

Magnetization isotherms at 1.8 K for three different orientations are shown in Fig. 4(b), where the small anisotropy between the  $\mathbf{ac}$  plane and the  $\mathbf{b}$  axis is clearly revealed. dHvA oscillations in all three directions are clearly observed in field as low as 5 kOe at  $T = 1.8$  K, superimposed on a linear diamagnetic background. These oscillations were detected for  $H < 70$  kOe for temperatures as high as 30 K. These observations imply very low conduction electron scattering and point toward the very high quality of the samples used in

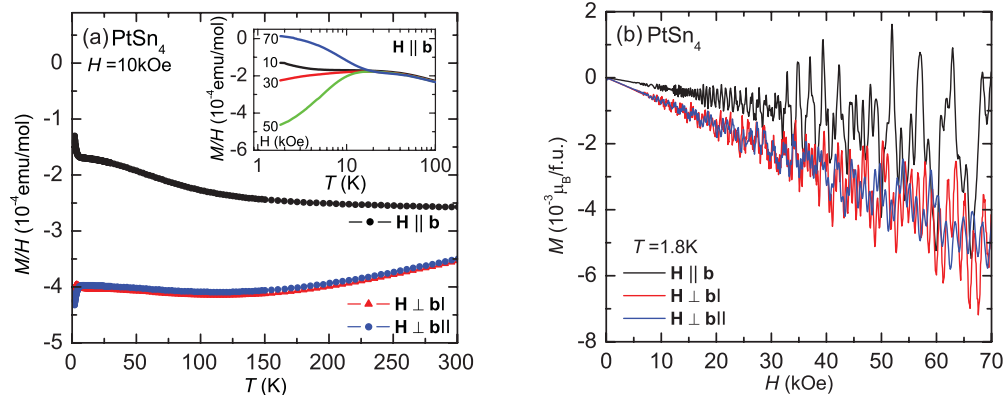


FIG. 4. (Color online) (a) Temperature-dependent  $M(T)/H$  of  $\text{PtSn}_4$  for  $\mathbf{H} \parallel \mathbf{b}$ ,  $\mathbf{H} \perp \mathbf{bl}$ , and  $\mathbf{H} \perp \mathbf{blI}$ . (Inset) Low-temperature  $M(T)/H$  for  $\mathbf{H} \parallel \mathbf{b}$ . (b) Magnetization isotherms of  $\text{PtSn}_4$  for  $\mathbf{H} \parallel \mathbf{b}$ ,  $\mathbf{H} \perp \mathbf{bl}$ , and  $\mathbf{H} \perp \mathbf{blI}$  at 1.8 K.

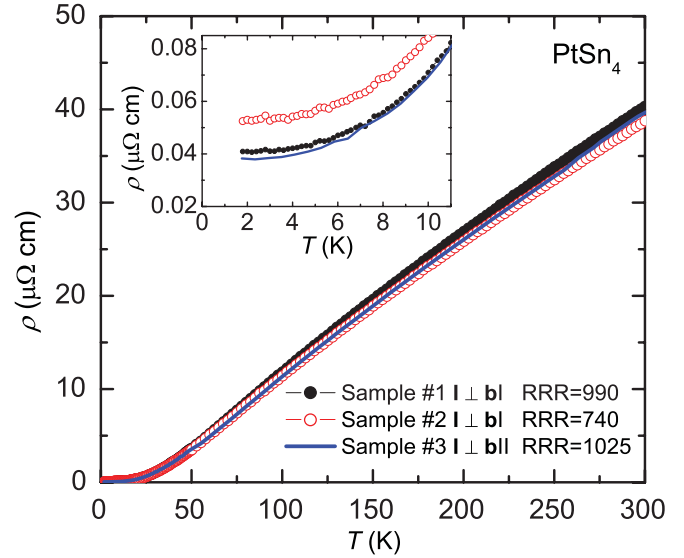


FIG. 5. (Color online) Zero-field electrical resistivity of  $\text{PtSn}_4$  for three samples. The current  $\mathbf{I}$  was applied parallel to the plane of longer axis ( $\mathbf{I} \perp \mathbf{bl}$ ) and shorter axis ( $\mathbf{I} \perp \mathbf{blI}$ ). Inset shows the low-temperature resistivity. For details see text.

the present study. Detailed analysis of the dHvA oscillations will be presented below.

### C. Resistivity

The electrical resistivity,  $\rho(T)$ , of  $\text{PtSn}_4$  was measured from 1.8 to 305 K and found to be metallic (Fig. 5); for  $50 \text{ K} < T < 300 \text{ K}$   $\rho(T)$  decrease in a roughly linear fashion with decreasing temperature, below 50 K  $\rho(T)$  starts to saturate with a very small residual resistivity after passing through a weak slope change, and below 7 K  $\rho(T)$  is proportional to  $T^2$ . Figure 5 shows  $\rho(T)$  of three  $\text{PtSn}_4$  samples where the electrical current was applied parallel to the plane of crystals,  $\mathbf{I} \perp \mathbf{b}$ , as mentioned in the experimental section. The labels  $\mathbf{I} \perp \mathbf{bl}$  and  $\mathbf{I} \perp \mathbf{blI}$  indicate that the applied current is parallel to the longer and shorter orthogonal edge facets of the crystal, respectively. All three samples have similar values of the resistivity at 300 K as well as similar residual resistivities, indicating that the  $\mathbf{ac}$  plane anisotropy

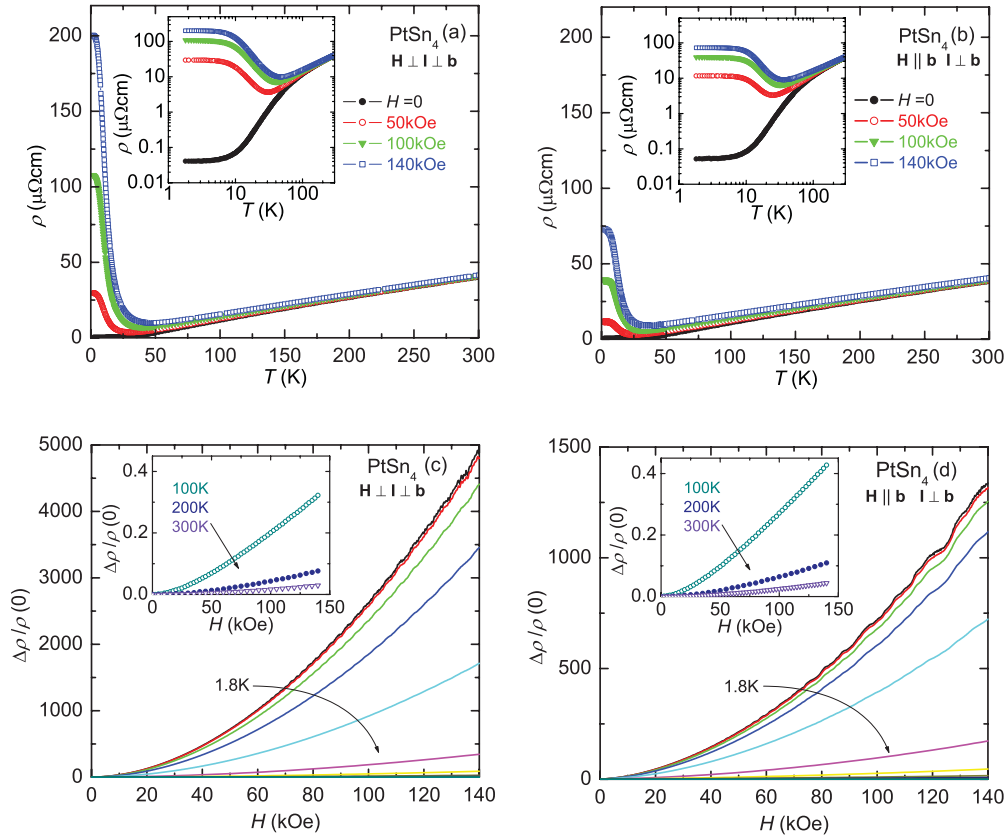


FIG. 6. (Color online) Resistivity measurements as a function of temperature and field on PtSn<sub>4</sub> single crystals. Temperature-dependent resistivity for (a) an applied field along the **ac** plane (**H** ⊥ **b**) and (b) along the **b** axis (**H** ∥ **b**). Insets (a) and (b) are as follows:  $\rho(T)$  vs  $\log(T)$  plot. Magnetic field-dependent resistivity  $\Delta\rho/\rho(0)$  for (c) **H** ⊥ **b** and (d) **H** ∥ **b** at  $T = 1.8, 3, 5, 7, 10, 15, 20, 25, 30, 50, 100, 200,$  and  $300$  K (top to bottom). Insets (c) and (d) are as follows:  $\Delta\rho/\rho(0)$  at  $T = 100, 200,$  and  $300$  K. The electrical current was applied in the **ac** plane (**I** ⊥ **b**) for all measurements.

of PtSn<sub>4</sub> is small. The residual resistivity  $\rho_0$  and the residual resistivity ratio (RRR) determined by  $\rho(300\text{ K})/\rho(2\text{ K})$  are  $\rho_0 = 0.041\ \mu\Omega\text{cm}$  and  $\text{RRR} = 740$ ,  $\rho_0 = 0.053\ \mu\Omega\text{cm}$  and  $\text{RRR} = 990$ , and  $\rho_0 = 0.038\ \mu\Omega\text{cm}$  and  $\text{RRR} = 1025$  for samples No. 1, No. 2, and No. 3, respectively. The very low residual resistivity and the large RRR indicate the exceptional quality of samples. The power law analysis of the resistivity with the relation  $\rho(T) = \rho_0 + AT^2$  at low temperatures results the small coefficient of  $A \simeq 2 \times 10^{-4}\ \mu\Omega\text{cm}/\text{K}^2$ . The small value of the electron-electron scattering coefficient, denoted by  $A$ , is consistent with the small effective mass estimated from specific heat coefficient  $\gamma \sim 4\ \text{mJ}/\text{mol K}^2$ ;  $A/\gamma^2 \simeq 1.25 \times 10^{-5}\ \mu\Omega\text{cm}(\text{mol K}/\text{mJ})^2$ .

Samples were selected for transverse MR measurements with the field oriented parallel to the **b** axis (sample No. 1, **H** ∥ **b**) and perpendicular to the **b** axis (sample No. 2, **H** ⊥ **b**). Figures 6(a) and 6(b) show the temperature dependence of the resistivity at  $H = 0, 50, 100,$  and  $140$  kOe. The field dependence of the resistivity for **H** ⊥ **b** is larger than that for **H** ∥ **b** at low temperatures:  $\rho(1.8\text{ K}, 140\text{ kOe})$  for **H** ⊥ **b** is approximately a factor of 3 larger than that for **H** ∥ **b**. In a given field,  $\rho(T)$  increase rapidly as temperature decreases from 50 to 10 K, and then below 10 K  $\rho(T)$  is saturated to a constant value as can be more clearly seen in the log-log plot (insets). This is, of course, the same temperature region ( $T < 10$  K) that the  $\rho(T)$  saturates to the residual resistivity in zero field.

As shown in Figs. 6(a) and 6(b), the resistivity has a relatively weak field dependence above 50 K, but depends strongly on magnetic field below this temperature. The size and anisotropy of MR can be seen explicitly in Figs. 6(c) and 6(d). The relative change of the MR as a function of magnetic field is plotted by the typical definition of MR,<sup>8</sup>  $\frac{\Delta\rho}{\rho(0)} = \left[ \frac{\rho(H) - \rho(H=0)}{\rho(H=0)} \right]$ , where  $\rho(H=0)$  is the zero field resistivity for each given isotherms. Interestingly, there is no evidence of the saturation of MR for either direction in temperature and field range measured. At  $T = 1.8\text{ K}$  and  $H = 140\text{ kOe}$ , a huge MR effect of  $\simeq 5 \times 10^5\%$  for **H** ⊥ **b** and  $\simeq 1.4 \times 10^5\%$  for **H** ∥ **b** can be obtained. Note that at 300 K and 140 kOe the observed MR is small;  $\Delta\rho/\rho(0) \sim 3\%$  for **H** ⊥ **b** and  $\Delta\rho/\rho(0) \sim 4\%$  for **H** ∥ **b**. The transverse MR is almost proportional to  $H^2$  over the field range measured. The size of MR in PtSn<sub>4</sub> is comparable, but smaller, than Bi and much larger than that of Cu.<sup>8,12</sup> There are SdH oscillations superimposed on the MR. The amplitude of the oscillations increases with increasing field and decreasing temperature. Detailed analysis of the SdH data will be presented below.

#### D. Hall coefficient and thermoelectric power

The transport properties of PtSn<sub>4</sub> are further characterized by measurements of the Hall resistivity  $\rho_H$  and thermoelectric power (TEP,  $S$ ). Figure 7(a) shows the magnetic

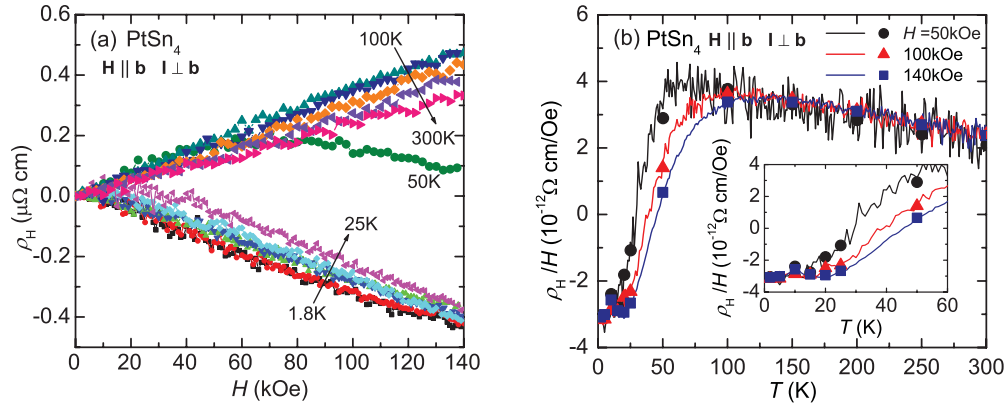


FIG. 7. (Color online) (a) Hall resistivity ( $\rho_H$ ) of PtSn<sub>4</sub> measured at  $T = 100, 150, 200, 250, 300,$  and  $50$  K (top to bottom) and  $T = 1.8, 5, 10, 15, 20,$  and  $25$  K (bottom to top). (b) Hall coefficient,  $R_H = \rho_H/H$ , of PtSn<sub>4</sub> at  $H = 50, 100,$  and  $140$  kOe. Solid lines are obtained from the temperature dependence of  $\rho_H$  and solid symbols are taken from the field dependence of  $\rho_H$ . Inset shows  $R_H$  at low temperatures. The electrical current was applied in the **ac** plane ( $\mathbf{I} \perp \mathbf{b}$ ) and the magnetic field was applied along the **b** axis ( $\mathbf{H} \parallel \mathbf{b}$ ) for all measurements.

field-dependent  $\rho_H$  measured at several temperatures. At high temperatures,  $\rho_H$  manifests a linear field dependence with positive values. As temperature decreases below 100 K, through 50 K, to 25 K,  $\rho_H$  becomes nonlinear in the magnetic field. For example, the 50 K  $\rho_H$  curve is positive at low fields, and then turns toward negative values with increasing magnetic field. Below 25 K,  $\rho_H$  is negative and again has a linear field dependence that is comparable to the 300 K curve.

The temperature-dependent Hall coefficient,  $R_H = \rho_H/H$ , of PtSn<sub>4</sub> is presented in Fig. 7(b). Above 75 K  $R_H$  depends weakly on temperature with a positive value that indicates hole-like carriers dominate its electrical transport. Within the framework of a one-band approximation, the carrier density  $n \simeq 2.6 \times 10^{28} \text{ m}^{-3}$  ( $R_H \sim 2.4 \times 10^{-12} \Omega \text{ cm/Oe}$ ) at 300 K is very close to the carrier concentration of copper  $\simeq 8.9 \times 10^{28} \text{ m}^{-3}$ .<sup>13</sup> Since the measured  $R_H$  is an average of the holes and electrons weighted by their mobilities, it will be shown below (in the discussion section), these data are treated more adequately within the framework of a two-band model. Upon cooling below 50 K, a sign reversal of  $R_H$ , from positive to negative, is found around 25 K for  $H = 50$  kOe and 45 K

for  $H = 140$  kOe. With further cooling  $R_H$  becomes roughly constant, saturating near  $\sim -3 \times 10^{-12} \Omega \text{ cm/Oe}$ .

TEP data of PtSn<sub>4</sub> are consistent, in a qualitative way, with the behavior observed in  $R_H$ . Figures 8(a) and 8(b) show the temperature and field dependence of TEP;  $S(T, H)$ . In zero field, the value of TEP is positive at high temperatures signifying that hole-type carriers dominate the thermoelectric transport in this material. Upon cooling, TEP shows a sign reversal around 30 K, and then exhibits a broad extremum around 20 K ( $\approx \Theta_D/11$ ) which is possibly due to the phonon drag.<sup>14</sup> Below 50 K,  $S(T)$  follows the same qualitative behavior as  $R_H$ ; it decreases sharply and changes sign. Below 10 K the absolute value of TEP starts to approach zero. The magnetothermoelectric power (MTEP) as a function of temperature is shown in Fig. 8(a). Above 100 K, MTEP is positive and depends weakly on field, whereas increasingly large MTEP effect appears below this temperature. As magnetic field increases a greatly enhanced MTEP is seen between 2 and 100 K, dominated by the peak-like structure centered around  $\sim 13$  K and shifting the sign reversal temperature to higher values as field increases; changing from 33 K for  $H = 0$  to

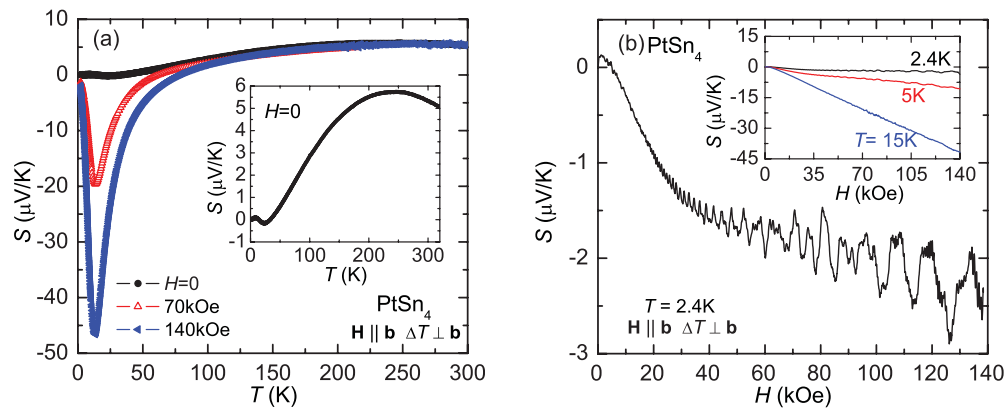


FIG. 8. (Color online) (a) Temperature-dependent thermoelectric power (TEP,  $S$ ) of PtSn<sub>4</sub> at  $H = 0, 70,$  and  $140$  kOe. Inset shows zero-field TEP. (b) Magnetic field dependence of the TEP of PtSn<sub>4</sub> at  $T = 2.4$  K, showing quantum oscillation for  $H > 20$  kOe. Inset shows the TEP at  $T = 2.4, 5,$  and  $15$  K. The magnetic field was applied along the **b** axis ( $\mathbf{H} \parallel \mathbf{b}$ ) and the temperature difference across the sample was generated in the **ac** plane ( $\Delta T \perp \mathbf{b}$ ) for all measurements.

78 K for  $H = 140$  kOe. The peak position remains the same as the magnetic field increases from 70 kOe to 140 kOe, located near the temperature of phonon-drag feature observed in zero field.

TEP as a function of field is plotted in Fig. 8(b). Quantum oscillations in the  $T = 2.4$  K data are clearly seen for applied fields greater than 20 kOe. At higher temperature (inset) the absolute value of TEP increases linearly with increasing field. The quantum oscillations have been observed in the TEP of many metallic elements such as zinc,<sup>15</sup> semimetal Bi,<sup>16</sup> however, compared to dHvA and SdH, have been rarely measured for intermetallic compounds.<sup>17</sup>

#### IV. DISCUSSION

PtSn<sub>4</sub> is an ordered intermetallic compound which manifest itself as exceptionally low  $\rho_0$ , high RRR, large MR effect, and quantum oscillations found in  $\rho(H)$ ,  $M(H)$ , and  $S(H)$  over wide ranges of temperature and magnetic field. The resistivity, Hall coefficient, and TEP of PtSn<sub>4</sub> depend strongly on magnetic field and temperature.  $R_H$  and  $S(T)$  indicate a sign reversal with decreasing temperature, which suggests that two different types of carriers with opposite sign are present in this compound. A common interpretation of such a sign reversal is that, as the temperature is lowered, electron and hole scattering rates change in a different manner, leading to a variation of the mobility of charge carriers. Such a sign change of  $R_H$  is also observed in many materials, such as Al and Bi.<sup>8</sup>

Based on the experimental results a two-band model is used to determine the main physical quantities. If there are two bands crossing the Fermi surface, the MR, Hall coefficient, and TEP can be expressed by the following equations,<sup>12,18</sup>

$$\begin{aligned} \frac{\Delta\rho(H)}{\rho(0)} &= \frac{1}{e} \frac{(1 + \mu_e^2 H^2)(1 + \mu_h^2 H^2)}{n_e \mu_e (1 + \mu_h^2 H^2) + n_h \mu_h (1 + \mu_e^2 H^2)}, \\ \frac{\rho_H}{H} &= \frac{1}{e} \frac{n_h \mu_h^2 - n_e \mu_e^2}{(n_h \mu_h + n_e \mu_e)^2} = \frac{1}{e} \frac{n_h - n_e (\mu_e/\mu_h)^2}{(n_h + n_e (\mu_e/\mu_h))^2}, \\ S &= \frac{\pi^2 k_B^2 T}{3e} \left( \frac{\partial \ln d_0 N_e}{\partial E} + \frac{\partial \ln d_0 N_h}{\partial E} \right)_{E=E_F}, \end{aligned}$$

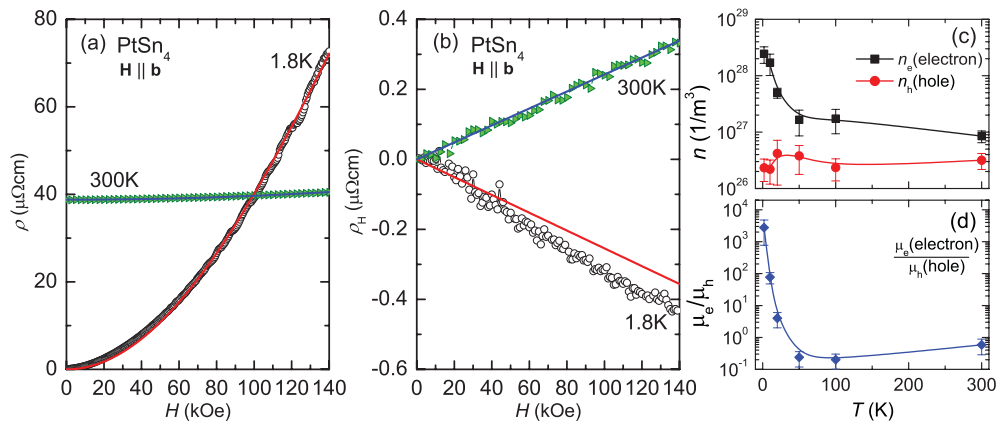


FIG. 9. (Color online) (a) Electrical resistivity and (b) Hall resistivity as a function of field at 1.8 and 300 K for  $\mathbf{H} \parallel \mathbf{b}$ . Solid lines are fits to the data using two-band model (see text for details). (c) Electron (squares) and hole (circles) concentrations as a function of temperature, as determined from a two-band model fit to electrical resistivity and Hall resistivity. (d) Ratio  $(\mu_e/\mu_h)$  between the hole and electron mobility as a function of temperature, as determined from the two-band model fit. Lines in (c) and (d) are guides to the eye.

where  $n_x$  are the carrier densities,  $\mu_x$  the mobilities, and  $N_x$  the density of states at the Fermi surface of electrons (e) and holes (h). The diffusion constant  $d_0$  in TEP is connected to the conductivity for simple form  $\sigma = ne^2\tau/m^* = d_0N$  where  $\tau$  is the relaxation time and  $m^*$  is the effective mass of carrier.

In the analysis of data the linear field dependence of  $\rho_H$  and the quadratic field dependence of MR is only considered, neglecting higher order terms in magnetic field. From the fit to the measured MR, using above equations, as shown in Fig. 9(a), the density of charge carriers and mobilities are estimated, and with these fit parameters  $\rho_H$  are reproduced as shown in Fig. 9(b). At 300 K the carrier concentrations are of a similar order of magnitude, as shown in Fig. 9(c), but the hole mobility is somewhat higher than the electron mobility. As the temperature is lowered below 50 K, the electron concentration greatly exceeds the hole concentration, by two orders of magnitude, and the electron mobility is also vastly enhanced: Such a temperature-dependent change in carrier density could be related to the thermal depopulation of hole-like pockets just above the Fermi level. Thus, electrons and holes are scattered in a different manner, as the temperature is lowered. As a consequence, the  $\mu_e/\mu_h$  ratio is highly temperature dependent as shown in Fig. 9(d). This is the origin of the sign reversal in the  $R_H$  and  $S(T)$ . From the above equations in the two-band model  $S(T)/T$  is expected to be similar to  $R_H$ . The temperature dependencies of the  $S(T)/T$  and  $R_H$  are shown in Fig. 10. This plot shows that the transport properties are dominated by hole-like carriers at high temperature and by electron-like carriers at low temperature. The low temperature upturn in  $S(T)/T$  is related to the phonon drag. The large change in  $S(T)/T$  and  $R_H$  involving a sign reversal around 30 K is caused by the enhancement of the ratio  $\mu_e/\mu_h$ . Note that the resistivity also shows a drastic change of scattering mechanism in the same temperature region which can be seen in the  $d\rho(T)/dT$  curve, as shown in the inset of Fig. 10.

In a simple case of a metal with electrons and holes, one may find the simple relation  $\Delta\rho/\rho(0) \sim (\omega_c\tau)^2$  where  $\omega_c = eH/m^*c$  is the cyclotron frequency. This relation also holds for PtSn<sub>4</sub>. From Fig. 6, no clear indication of saturation in MR is observed in either field orientation,  $\mathbf{H} \parallel \mathbf{b}$  or  $\mathbf{H} \perp \mathbf{b}$ .

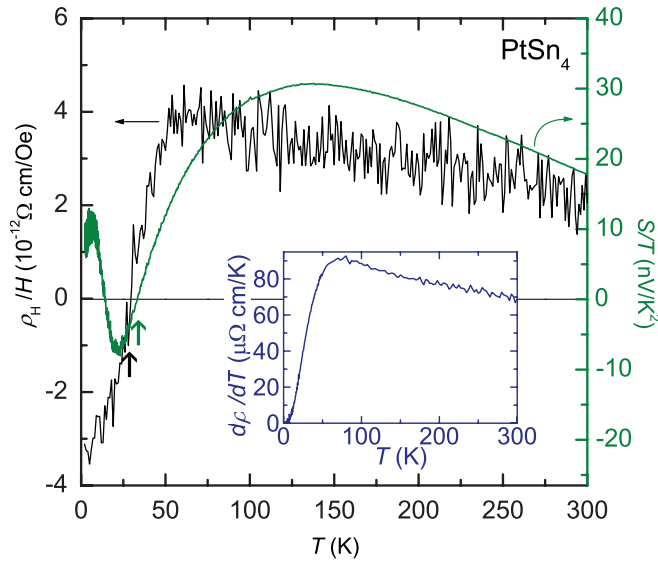


FIG. 10. (Color online) Hall coefficient ( $R_H$ , left axis), TEP [ $S(T)/T$ , right axis], and resistivity [ $d\rho(T)/dT$ , inset] of  $\text{PtSn}_4$  as a function of temperature. Vertical arrows indicate the sign reversal temperature corresponding to  $R_H = 0$  and  $S(T)/T = 0$ .

The relative MR of many metals and semimetals can be represented by the form, commonly referred to as Kohler's rule,<sup>8</sup>  $\Delta\rho/\rho(0) = F[H/\rho(0)]$ , where  $F(H)$  usually follows a power law, depending on the geometrical configurations and on the materials. The normal MR in fixed orientation of the crystal either saturates at high fields or increases as  $H^2$ .<sup>8,12</sup> As shown in Fig. 11,  $\text{PtSn}_4$  has a field dependence of  $\Delta\rho/\rho(0) \simeq H^{1.8}$  for both orientations of field, where all resistivity curves collapse onto a single line for each orientation. At high temperatures and very low-field regime at low temperatures, although MR curves show a scaling behavior,  $\Delta\rho/\rho(0)$  curves do not follow  $H^{1.8}$  dependence shown in the inset of Fig. 11 for  $\mathbf{H} \perp \mathbf{b}$ .

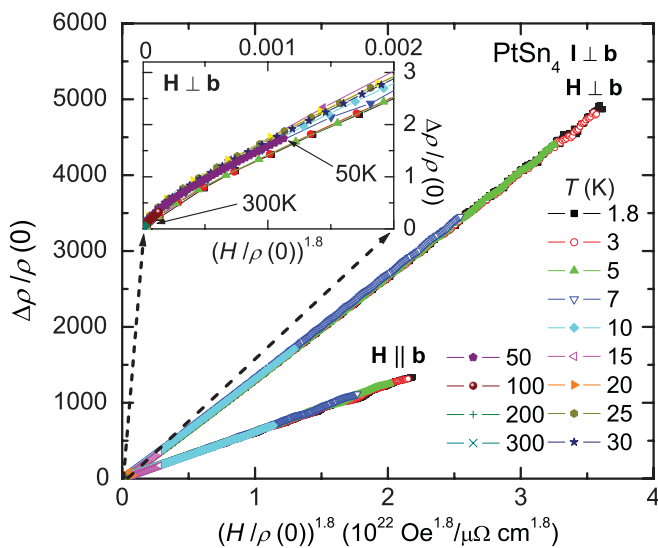


FIG. 11. (Color online) A Kohler plot for  $\text{PtSn}_4$  using  $\Delta\rho/\rho(0) = F[H/\rho(0)] \simeq H^{1.8}$ . Inset shows a Kohler plot at high temperatures for  $\mathbf{H} \perp \mathbf{b}$ .

In the two-band model, the experimental MR and Hall data can be explained by the  $\mu_e/\mu_h$  ratio and carrier density, where  $n_e$  shows a peculiar behavior;  $n_e \simeq n_h$  at 300 K and  $n_e \gg n_h$  at 2 K. Below 30 K  $\rho_H/H$  data are field independent and MR curves can be explained well with Kohler's rule. At 2 K the estimated value of  $n_e = 2.4 \times 10^{28} \text{ m}^{-3}$  is close to the carrier concentration  $n \sim 2 \times 10^{28} \text{ m}^{-3}$  in a single-band approximation. Hence, at the base temperature we can assume that  $\text{PtSn}_4$  is like a single-band (electron-like) metal. Based on this assumption, the large MR effect in  $\text{PtSn}_4$  can be understood qualitatively by considering the quantity  $\omega_c\tau$  as well as the mean free path ( $l$ ). For the normal MR it is important to consider the quantity  $\omega_c\tau = H\sigma/nec$  which means the angle turned between collisions when a magnetic field is large enough to bend the trajectory of carriers into helices due to the Lorentz force. It has been shown that in order to have a large MR effect, generally the criterion  $\omega_c\tau \gg 1$  should be satisfied.<sup>8</sup> At low temperatures it is clear from the small residual resistivity ( $\rho_0 \sim 0.04 \mu\Omega \text{ cm}$ ) as well as the clear and persistent dHvA oscillation that the mean free path of carriers near the Fermi surface must be long. At the first stage the mean free path can be estimated by using the simple approximation  $\rho l = (3\pi^2/n^2)^{1/3}\hbar/e^{28}$  with  $n$  of carriers obtained from  $R_H$ . At 2 K the estimated mean free path of carriers is about  $3 \mu\text{m}$ , and at 300 K, the mean free path of carriers is much shorter than 2 K, estimated to be  $\sim 3 \text{ nm}$ . The size of the MR effect for  $\mathbf{H} \parallel \mathbf{b}$  is determined by  $\omega_c\tau \simeq 6.2 \times 10^{-4}H$  at 300 K and  $\omega_c\tau \simeq 0.6H$  at 2 K; the  $\omega_c\tau$  at 2 K is about  $10^3$  times higher than  $\omega_c\tau$  at 300 K, and the carriers are turned easily at 2 K between collisions which is enough to change the conduction process. Hence, the key to realizing a large MR effect of  $\text{PtSn}_4$  is the large  $\omega_c\tau$ , which is directly related to the sample quality. Although a single (spherical)-band approximation may not be valid for the  $\text{PtSn}_4$  system, the large MR effect can be understood in a qualitative way using a single-band model, fundamentally due to the unusually high  $\mu_e/\mu_h$  ratio and  $n_e \gg n_h$  below 30 K. In comparison, the carrier concentration of  $\text{PtSn}_4$  is similar to Cu, but  $m^*$  determined by dHvA and SdH oscillation (see below) is an order of magnitude smaller than Cu, and  $\omega_c\tau$  is about two orders of magnitude larger than Cu.<sup>19</sup> Note that, although the temperature dependence of transport properties in  $\text{PtSn}_4$  can be explained qualitatively in the two-band model, the temperature dependence of the carrier concentration below 50 K (in two-band model calculation) is unusual, so the realistic band structure and a three- or four-band fit need to be considered.

The observed behavior of  $\Delta\rho/\rho(0) \sim H^2$  and  $R_H \sim H^1$  is close to what is expected for an ordinary metallic compound with no open orbits. Although the MR is not simply related to the topology of the Fermi surface, MR data measured for both  $\mathbf{H} \parallel \mathbf{b}$  and  $\mathbf{H} \perp \mathbf{b}$  indicate a significant anisotropy in the band structure. In a compensated metallic compound, no saturation is expected to be observed for either the transverse or longitudinal MR, where MR shows a deviation from quadratic field dependence. For instance, the transverse MR of the  $R\text{AgSb}_2$  ( $R = \text{rare earth}$ ) series shows a deviation from quadratic field dependence, where  $\Delta\rho/\rho(0)$  ranges between  $H^{0.8}$  and  $H^{1.5}$ .<sup>20</sup> In a similar manner the  $R\text{Sb}_2$  compounds have power laws of  $\Delta\rho/\rho(0)$  varying from 1 to 1.3.<sup>21</sup>

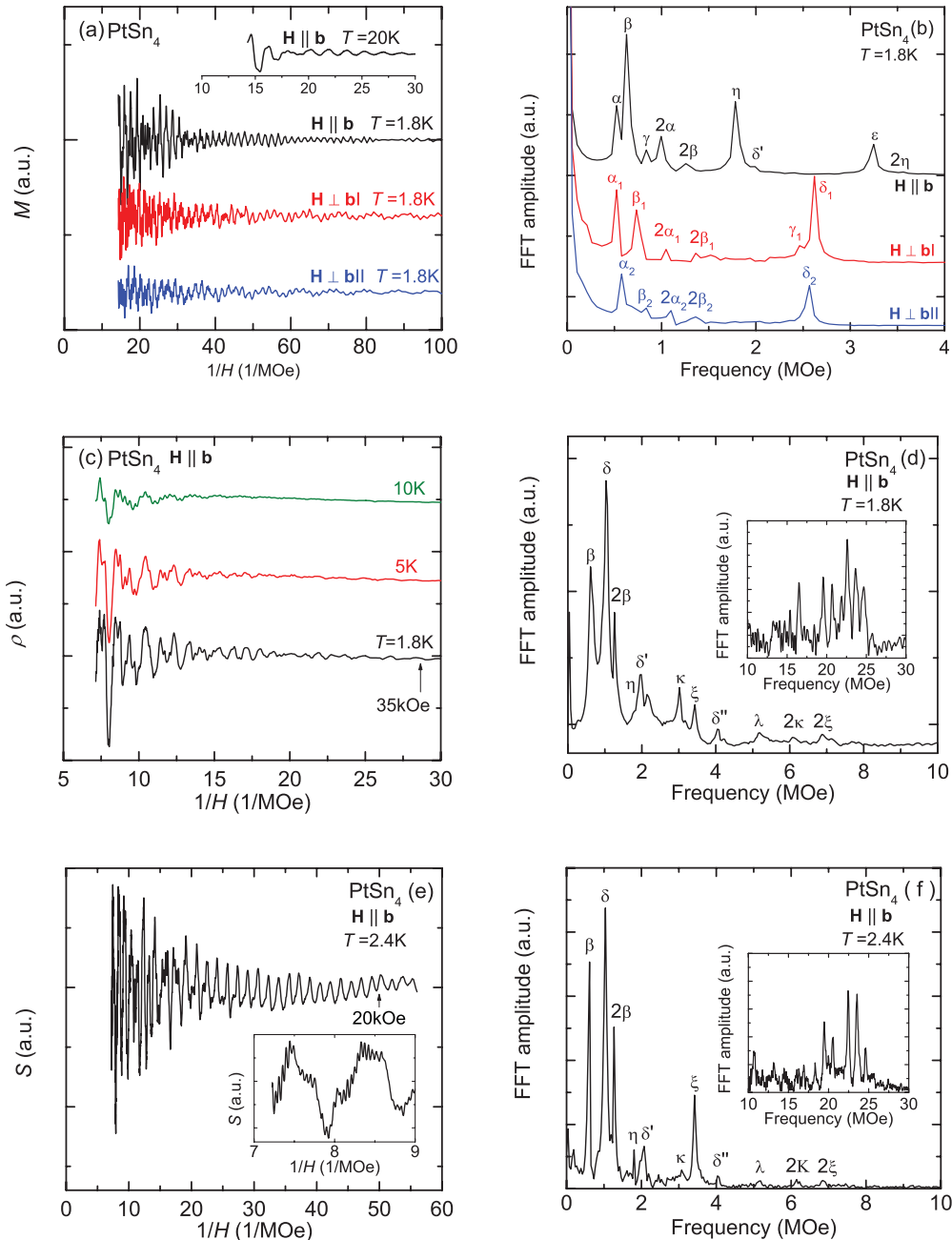


FIG. 12. (Color online) (a) Magnetization isotherms of PtSn<sub>4</sub> at  $T = 1.8$  K for three different orientations, plotted as a function of  $1/H$ . Inset shows a magnetization isotherm at 20 K for  $\mathbf{H} \parallel \mathbf{b}$ . (b) FFT spectra of dHvA data for three different orientations. (c) Resistivity of PtSn<sub>4</sub> at 1.8, 5, and 10 K for  $\mathbf{H} \parallel \mathbf{b}$ . (d) FFT spectra of SdH data at  $T = 1.8$  K. Inset shows the FFT spectra in the high frequency region. (e) TEP of PtSn<sub>4</sub> at  $T = 2.4$  K for  $\mathbf{H} \parallel \mathbf{b}$ . Inset shows the TEP in the high field region. (f) FFT spectra of TEP data at  $T = 2.4$  K. Inset shows the FFT spectra in the high frequency region.

The size of MR of PtSn<sub>4</sub> at low temperatures is comparable to or even greater than the largest giant magnetoresistance (GMR)<sup>22–24</sup> and colossal magnetoresistance (CMR)<sup>25–29</sup> materials. One of the several technological applications based on large MR effects at low temperatures will be the magnetic field sensor. The MR effect in PtSn<sub>4</sub> may be suitable for detecting relatively small magnetic fields or field changes for fields up to at least 140 kOe. At 1.8 K and 140 kOe, a huge MR effect of  $\simeq 5 \times 10^5$  % for  $\mathbf{H} \perp \mathbf{b}$  and  $\simeq 1.4 \times 10^5$  % for  $\mathbf{H} \parallel \mathbf{b}$  can be obtained. If we assume that the observed MR

continues without saturation, the very high sensitivity and a large dynamic range (below 30 K) can potentially be used to detect magnetic fields generated by pulsed fields ( $H > 30$  T) and superconducting magnets (20 T). Among intermetallic compounds, the highly anisotropic LaSb<sub>2</sub><sup>21</sup> has been proposed to use as a high magnetic field sensor in either a transverse MR or a Hall configuration.<sup>30</sup> It needs to be noted that, when intermetallic compounds are used as a magnetic field sensor, in particular, in pulsed fields (also oscillations are not good for the sensor), eddy current heating needs to be considered.



TABLE I. Frequencies and effective masses  $m^*$  obtained from the dHvA [ $M(H)$ ], SdH [ $\rho(H)$ ], and TEP [ $S(H)$ ] oscillations.  $m_e$  is the bare electron mass.

	$\mathbf{H} \parallel \mathbf{b}$					$\mathbf{H} \perp \mathbf{bI}$		$\mathbf{H} \perp \mathbf{bII}$	
	dHvA (MOe)	$m^*/m_e$	(MOe)	SdH $m^*/m_e$	$S(H)$ (MOe)	dHvA (MOe)		dHvA (MOe)	
$\alpha$	0.52	0.11				$\alpha_1$	0.52	$\alpha_2$	0.57
$\beta$	0.63	0.13	0.61	0.16	0.61	$\beta_1$	0.73	$\beta_2$	0.68
$\gamma$	0.84	0.16				$2\alpha_1$	1.04	$2\alpha_2$	1.10
$2\alpha$	0.99	0.23				$2\beta_1$	1.41	$2\beta_2$	1.36
$\delta$			1.03	0.29	1.03	$\gamma_1$	2.46		
$2\beta$	1.26		1.26	0.31	1.27	$\delta_1$	2.62	$\delta_2$	2.57
$\eta$	1.78	0.15	1.79		1.81	$2\gamma_1$	4.93		
$\delta'$	1.99		1.98	0.30	2.07	$2\delta_1$	5.71		
$\varepsilon$	3.25	0.29				$\lambda_1$	7.91		
$2\eta$	3.56					$\psi_1$	9.33		
$\delta''$	4.03		4.08		4.07	$\nu_1$			
$2\varepsilon$	6.45								
$\kappa$			3.02	0.16	3.07				
$\xi$			3.44	0.36	3.42				
$\lambda$			5.19		5.18				
$2\kappa$			6.11		6.14				
$2\xi$			6.87		6.83				

In addition to the large MR effect, TEP also shows a large magnetic field dependence. Figure 8 shows that, in the presence of magnetic field, a large enhancement of  $S(T)$  for PtSn<sub>4</sub> is observed at low temperatures. Such a large change of MTEP with the applied field is reported in a few materials, such as noble metals,<sup>14</sup> doped semiconductors InSb and AgTe,<sup>31,32</sup> and materials with charge density wave order LaAgSb<sub>2</sub>.<sup>17</sup> For the semiconductor InSb,<sup>31</sup> a very large MTEP was induced by the different mobility between minority and majority carriers when acoustic phonon scattering dominates. Additionally, the GMR multilayers, granular films,<sup>33</sup> and the CMR manganites<sup>34</sup> have been also reported to have large MTEP. Among these examples, the observed absolute values of  $\Delta S = S(H) - S(0)$  in Ag<sub>2- $\delta$</sub> Te,<sup>32</sup> which are an order of higher than other materials, suggest that this effect may be basically due to disorder and band crossings. Compared with those large MTEP materials, the enhanced TEP of PtSn<sub>4</sub> in magnetic field can be understood by considering the mobility change of charge carriers with electron-phonon scattering. It can be supported by the fact that  $S(T)$  at 70 kOe and 140 kOe shows the peaklike structure near  $\Theta_D/11$  and a similar temperature dependence between  $S(T)/T$  and  $R_H$  can be explained with the two-band model (Fig. 10).

Oscillatory effects have been observed throughout our measurements, at remarkably low fields and high temperatures. In Fig. 12(a) typical dHvA data sets for PtSn<sub>4</sub> taken at 1.8 K for the three different directions of applied field are displayed, where the linear background magnetization has been subtracted. The dHvA oscillations are observed over a wide range of temperatures for all field directions. The inset of Fig. 12(a) shows an example of the dHvA oscillation for  $\mathbf{H} \parallel \mathbf{b}$  at 20 K. The fast Fourier transform (FFT) of these data, shown in Fig. 12(b), reveals that these oscillations result from several independent frequencies in  $1/H$ , indicating many extremal

Fermi surface cross-sectional areas. The obtained frequencies are summarized in Table I. For  $\mathbf{H} \parallel \mathbf{b}$ , five frequencies can be clearly observed in the FFT spectrum corresponding to strong peaks at  $\alpha$ ,  $\beta$ ,  $\gamma$ ,  $\eta$ , and  $\varepsilon$ . The second harmonics of the frequencies  $\alpha$ ,  $\beta$ ,  $\eta$ , and  $\varepsilon$  and other frequencies  $\delta'$  and  $\delta''$  are also present as very weak peaks. FFT spectra of the oscillatory magnetization for applied fields perpendicular to the  $\mathbf{b}$  axis at 1.8 K are shown in the same figure. For  $\mathbf{H} \perp \mathbf{bI}$  three clear peaks and several weak signals are visible at  $\alpha_1$ ,  $\beta_1$ ,  $\gamma_1$ ,  $\delta_1$ ,  $2\alpha_1$ ,  $2\beta_1$ ,  $2\gamma_1$ , and  $2\delta_1$ . The frequencies of the oscillations observed for  $\mathbf{H} \perp \mathbf{bII}$  are similar to those observed for  $\mathbf{H} \perp \mathbf{bI}$ .

Quantum oscillations are also clearly observed in transport measurements. Figure 12(c) shows the resistivity data as a function of  $1/H$  at  $T = 1.8, 5,$  and  $10$  K for  $\mathbf{H} \parallel \mathbf{b}$ . SdH oscillations are clearly seen after subtracting the background MR ( $\propto H^{1.8}$ ). Since the signals comprise a superposition of several oscillatory components the data are most easily understood by taking the FFT as shown in Fig. 12(d). The FFT spectrum at  $T = 1.8$  K shows several frequencies including second harmonics. Additionally, several higher frequencies with smaller amplitude are resolved near 25 MOe as shown in the inset of Fig. 12(d). Figure 12(e) shows the TEP data as a function of  $1/H$ , subtracted background contributions using a third-order polynomial fit, taken at  $T = 2.4$  K for  $\mathbf{H} \parallel \mathbf{b}$ . The TEP has some distinct differences associated with quantum oscillations when compared with more conventional thermodynamic and transport measurements. Since specific heat, magnetization, resistivity, etc., all depend on density of states, quantum oscillations are associated with the periodic variation of this quantity. The unique aspect of TEP is that it depends on the derivative of the density of states evaluated at the Fermi energy.<sup>15,17</sup> Oscillations in TEP are clearly seen for  $H > 20$  kOe, where higher frequencies superimposed on lower frequencies are discernible for  $H > 100$  kOe as seen in

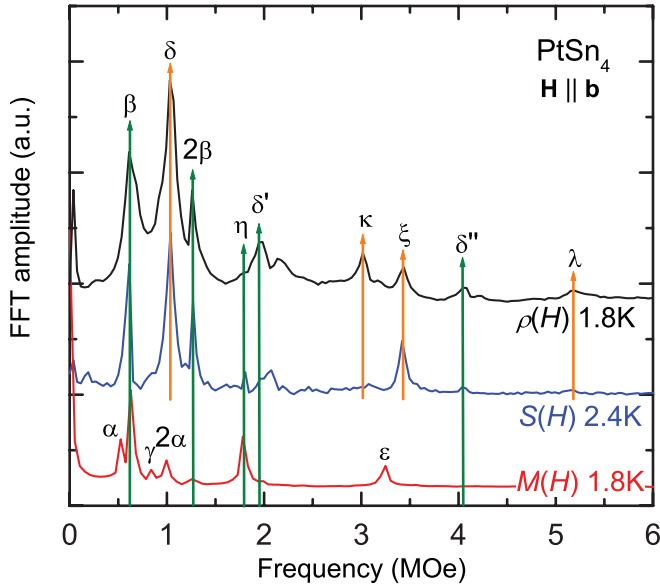


FIG. 13. (Color online) FFT spectra of the dHvA, SdH, and TEP data. Vertical arrows are guides to the eye.

the inset. In Fig. 12(f) the FFT spectrum shows clearly three frequencies with higher amplitude and several frequencies with lower amplitude. Besides these intense features and their harmonics, several other frequencies with much smaller amplitude are observed near 25 MOe as shown in the inset of Fig. 12(f), which is consistent with SdH results [Fig. 12(d) inset]. At least five frequency branches are visible, which will be related to the very large extremal cross-sectional areas of the Fermi surface. Branches of frequency below 10 MOe, clearly revealed in SdH and TEP oscillations, are listed in Table I.

The FFT spectra obtained from dHvA, SdH, and TEP are also plotted in Fig. 13 for comparison. As shown in the figure frequencies of  $\beta$ ,  $\eta$ ,  $\delta'$ , and  $\delta''$  in the FFT spectra corresponding to the SdH and TEP oscillation are consistent with the dHvA frequencies, where the high frequencies in SdH and TEP oscillations are clearly resolved in addition to relatively low frequencies (i.e., the higher order harmonics and the frequencies  $\kappa$ ,  $\xi$ , and  $\lambda$ ). However, frequencies of  $\alpha$ ,  $\gamma$ , and  $\varepsilon$  are only observable for dHvA measurements. Although the

frequency  $\delta = 1.03$  MOe in SdH and TEP spectrum is almost the same as  $2\alpha = 0.99$  MOe in dHvA spectrum, we assigned a different frequency since the first harmonics of this frequency are not seen in the SdH spectrum.

Quantum oscillations are discernible in magnetic fields as low as 5 kOe for  $M(H)$ , 35 kOe for  $\rho(H)$ , and 20 kOe for  $S(H)$  at the lowest temperature measured; these data imply very high quality samples as well as very small effective mass of conduction carriers. In order to estimate effective mass of the carriers, dHvA and SdH measurements were carried out at temperatures from 1.8 K to greater than 25 K. The frequencies in FFT spectra do not shift with temperature and most of the first harmonics of the frequencies were clearly observable as high as 20 K. The cyclotron effective mass of the carriers from the various orbits were determined by fitting the temperature-dependent amplitude of the oscillations to the Lifshitz-Kosevich formula:<sup>35</sup>

$$R_T = \frac{2\pi^2 p k T / \beta^* H}{\sinh(2\pi^2 p k T / \beta^* H)},$$

where  $\beta^* = e\hbar/m^*c$  and the mass  $m^*$  is the renormalized, or effective mass. The effective masses, calculated from the temperature-dependent amplitude of the oscillations are shown in Fig. 14; they range from  $m_\alpha \sim 0.1 m_e$  to  $m_\xi \sim 0.4 m_e$ , where  $m_e$  is the bare electron mass. These small effective masses are consistent with the results of specific heat measurements. The estimated effective masses are summarized in Table I. The effective mass associated with the second harmonic frequencies,  $2\alpha$  and  $2\beta$ , are twice that of first harmonics  $\alpha$  and  $\beta$ , confirming the assumption of these frequencies are higher harmonics. Although the value of the frequency  $\delta'$  is integer-multiple of either  $\alpha$  or  $\delta$ , it is not a higher harmonics of either  $\alpha$  or  $\delta$  because of the inconsistent effective mass (see Table I). Therefore,  $\delta'$  is an independent frequency, coming from an external orbit with the area close to  $2\delta$ .

As indicated by the dHvA oscillations, for all three orientations, the topology of the Fermi surface of PtSn<sub>4</sub> is complex. Therefore, band structure calculations have been performed within the full potential linearized augmented plane wave (FLAPW) method<sup>36</sup> within local density approximation (LDA).<sup>37</sup> A mesh of  $31 \times 31 \times 31 \vec{k}$  points was used for

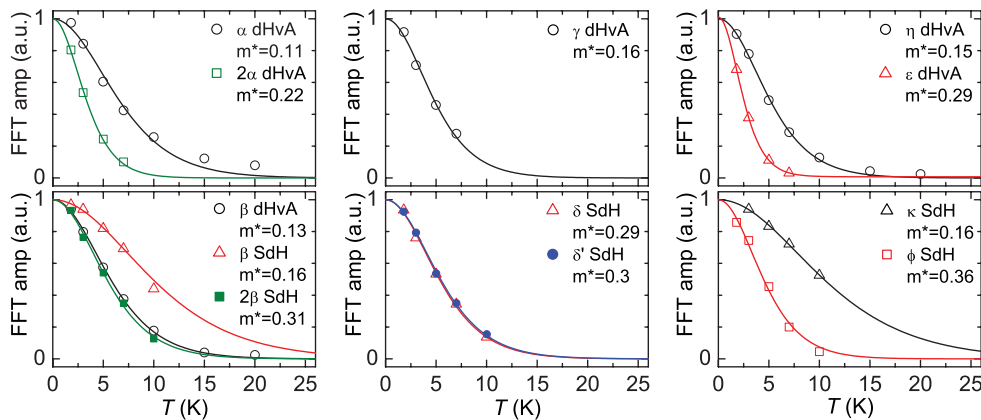


FIG. 14. (Color online) Temperature dependence of the dHvA and SdH amplitudes. Solid lines represent the fit to the Lifshitz-Kosevich formula.

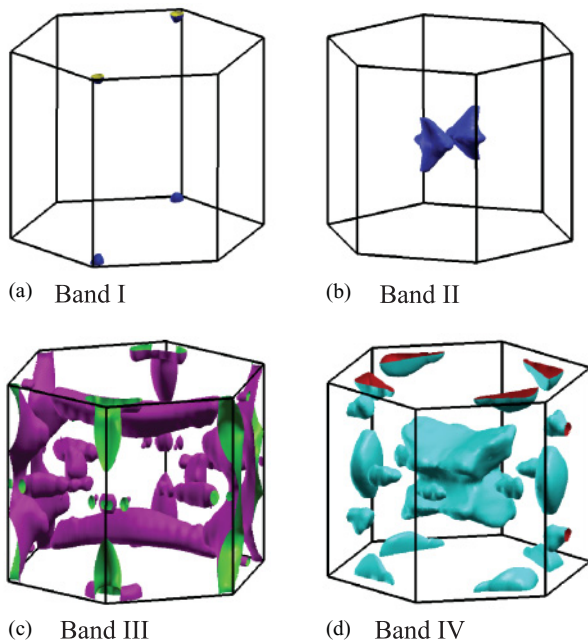


FIG. 15. (Color online) The theoretically calculated Fermi surface of PtSn<sub>4</sub>.

Brillouin zone integration and Fermi surface plot, with  $R_{MT} * K_{max} = 8$ ,  $R_{MT} = 2.3$  atomic units for both Pt and Sn. We used the room temperature experimental lattice constants and atomic positions. The original  $k$  mesh was interpolated onto a mesh 10 times as dense. In the calculated total and projected electronic density of states (DOS), the valence electron bands are derived from hybridized combination of Pt  $d$  and Sn  $s$  and  $p$  states; the electronic states in the energy interval between  $-6$  and  $-2$  eV are mostly by Pt  $d$  states, while the  $s$ -derived Sn component is distributed mostly below  $-6$  eV. The states at Fermi energy ( $E_F$ ) correspond mostly to  $p$  electrons of Sn with a small amount of Pt  $d$  states. The  $E_F$  is located in the local minimum of DOS anomaly. The last fact is usually associated with stability of particular crystal structure with given concentration of valence electrons. Similar to other semimetals, PtSn<sub>4</sub> compound has low DOS at  $E_F$  equals 2.8 St/eV f.u. and corresponding  $\gamma = 4$  mJ/mol K<sup>2</sup> which is consistent with experimental result. As can be recognized from the results of the calculations (Fig. 15), the Fermi surface of PtSn<sub>4</sub> is three dimensional, and very complex.

From the shape of Fermi surface many branches of frequency can be expected because the Fermi surface has multiple sheets. The relevant branches have not been compared with experimental frequencies, because there are many possibilities having similar size of extremal cross-sectional areas. The extremal areas in the low frequency region labeled as  $\alpha$ ,  $\beta$ ,  $\gamma$ , and  $\delta$  can be assigned to band I and the small spherical or ellipsoidal Fermi surface located near the zone boundary in band III and IV. The higher frequencies near 25 MOe can be related to two long, cylindrical and cucumber-shaped Fermi surface in band III or a large pillow-shaped Fermi surface in band IV. It would be necessary to measure frequencies as a function of angle between the crystallographic axes in order to make estimates of the Fermi surface topology.

## V. SUMMARY

High quality single crystals of PtSn<sub>4</sub> were grown from high temperature solution. Based on measurements of temperature and field dependencies of thermodynamic and transport properties, PtSn<sub>4</sub> can be classified as a metallic system with an axial magnetic and electronic anisotropy. In zero field the low residual resistivity and large resistivity ratio between 2 and 300 K indicate a high quality of PtSn<sub>4</sub> samples. The high quality of samples is further supported by the observation of very large MR and pronounced SdH and dHvA oscillations. The Hall resistivity and thermoelectric power measurement indicate a sign reversal below 50 K, caused by the dramatic change in the carrier density and mobility of the electron band. The application of a magnetic field causes not only a large magnetoresistance but also a large magnetothermoelectric power effect. These large magnetic field effects on transport properties are mainly due to different mobility changes for the different types of carriers. It is found that the Kohler's rule is valid in the transverse magnetoresistance of PtSn<sub>4</sub>, scaling with  $\Delta\rho/\rho(0) \simeq H^{1.8}$ . Finally, the observed quantum oscillations and an anisotropic field response on MR indicate a very complicate electronic structure of this compound.

## ACKNOWLEDGMENTS

Work at the Ames Laboratory was supported by the US Department of Energy Basic Energy Sciences under Contract No. DE-AC02-07CH11358.

\*Present address: Materials Science and Technology Division, Oak Ridge National Laboratory, Oak Ridge, TN 37831.

<sup>1</sup>H. Okamoto, *Desk Handbook Phase Diagrams for Binary Alloys* (ASM International, Materials Park, OH, 2000); *J. Phase Equilib.* **15**, 463 (1996).

<sup>2</sup>J. F. Kuhmann, C.-H. Chiang, P. Harde, F. Reier, W. Oesterle, I. Urban, and A. Klein, *Mater. Sci. Eng. A* **242**, 22 (1998).

<sup>3</sup>B. Kempf and S. Schmauder, *Gold Bull.* **31**, 51 (1998).

<sup>4</sup>T. Biggs, S. S. Taylor, and E. van der Lingen, *Platinum Met.* **49**, 2 (2005).

<sup>5</sup>C. R. Kanekar, K. R. P. Mallikarjuna Rao, and V. Udaya Shankar Rao, *Phys. Lett.* **19**, 95 (1965).

<sup>6</sup>R. Kubiak and M. Wolczyk, *J. Less-Common Met.* **109**, 339 (1985).

<sup>7</sup>Bernd Künnen, Dirk Niepmann, and Wolfgang Jeitschko, *J. Alloys Compd.* **309**, 1 (2000).

<sup>8</sup>A. B. Pippard, *Magnetoresistance in Metals* (Cambridge University Press, Cambridge, 1989).

<sup>9</sup>P. C. Canfield and Z. Fisk, *Philos. Mag. B* **65**, 1117 (1992).

<sup>10</sup>E. Mun, S. L. Bud'ko, M. S. Torikachvili, and P. C. Canfield, *Meas. Sci. Technol.* **21**, 055104 (2010).

- <sup>11</sup>F. Pobell, *Matter and Methods at Low Temperatures* (Springer, New York, 1996).
- <sup>12</sup>J. M. Ziman, *Electrons and Phonons* (Oxford, Clarendon Press, 1979).
- <sup>13</sup>C. Kittel, *Introduction to Solid State Physics* (John Wiley and Sons, New York, 1996).
- <sup>14</sup>F. J. Blatt, P. A. Schroeder, C. L. Foiles, and D. Greig, *Thermoelectric Power of Metals* (Plenum, New York, 1976).
- <sup>15</sup>R. Fletcher, *J. Phys. F* **11**, 1093 (1981).
- <sup>16</sup>J. H. Mangez, J.-P. Issi, and J. Heremans, *Phys. Rev. B* **14**, 4381 (1976).
- <sup>17</sup>E. Mun, S. Bud'ko, and P. Canfield, *J. Phys. Condens. Matter* **23**, 476001 (2011).
- <sup>18</sup>E. H. Sondheimer, *Proc. R. Soc. A* **193**, 484 (1948).
- <sup>19</sup>F. Seitz and D. Turnbull, *Solid State Physics: Advances in Research and Applications* (Academic Press, Waltham, 1963).
- <sup>20</sup>K. D. Myers, S. L. Bud'ko, I. R. Fisher, Z. Islam, H. Kleinke, A. H. Lacerda, and P. C. Canfield, *J. Magn. Magn. Mater.* **205**, 27 (1999).
- <sup>21</sup>S. L. Bud'ko, P. C. Canfield, C. H. Mielke, and A. H. Lacerda, *Phys. Rev. B* **57**, 13624 (1998).
- <sup>22</sup>M. N. Baibich, J. M. Broto, A. Fert, F. NguyenVanDau, F. Petroff, P. Etienne, G. Creuzet, A. Friederich, and J. Chazelas, *Phys. Rev. Lett.* **61**, 2472 (1988).
- <sup>23</sup>A. E. Berkowitz, J. R. Mitchell, M. J. Carey, A. P. Young, S. Zhang, F. E. Spada, F. T. Parker, A. Hutten, and G. Thomas, *Phys. Rev. Lett.* **68**, 3745 (1992).
- <sup>24</sup>J. Q. Xiao, J. S. Jiang, and C. L. Chien, *Phys. Rev. Lett.* **68**, 3749 (1992).
- <sup>25</sup>C. W. Searle and S. T. Wang, *Can. J. Phys.* **47**, 2703 (1969).
- <sup>26</sup>R. von Helmolt, J. Wecker, B. Holzapfel, L. Schultz, and K. Samwer, *Phys. Rev. Lett.* **71**, 2331 (1993).
- <sup>27</sup>K. Chahara, T. Ohno, M. Kasai, Y. Kanke, and Y. Kozono, *Appl. Phys. Lett.* **62**, 780 (1993).
- <sup>28</sup>S. Jin, T. H. Tiefel, M. McCormack, R. A. Fastnacht, R. Ramesh, and L. H. Chen, *Science* **264**, 413 (1994).
- <sup>29</sup>Y. Tokura, Y. Tomioka, H. Kuwahara, A. Asamitsu, Y. Moritomo, and M. Kasai, *J. Appl. Phys.* **79**, 5288 (1996).
- <sup>30</sup>D. P. Young, R. G. Goodrich, J. F. DiTusa, S. Guo, P. W. Adams, Julia Y. Chan, and Donovan Hall, *Appl. Phys. Lett.* **82**, 3713 (2003).
- <sup>31</sup>J. P. Heremans, C. M. Thrush, and D. T. Morelli, *Phys. Rev. Lett.* **86**, 2098 (2001); *Phys. Rev. B* **65**, 035209 (2001).
- <sup>32</sup>Young Sun, M. B. Salamon, M. Lee, and T. F. Rosenbaum, *Appl. Phys. Lett.* **82**, 1440 (2003).
- <sup>33</sup>J. Shi, K. Pettit, E. Kita, S. S. P. Parkin, R. Nakatani, and M. B. Salamon, *Phys. Rev. B* **54**, 15273 (1996).
- <sup>34</sup>M. Jaime, M. B. Salamon, K. Pettit, M. Rubinstein, R. E. Treece, J. S. Horwitz, and D. B. Chrisey, *Appl. Phys. Lett.* **68**, 1576 (1996).
- <sup>35</sup>D. Shoenberg, *Magnetic Oscillations in Metals* (Cambridge University Press, Cambridge, 1984).
- <sup>36</sup>P. Blaha *et al.*, "An augmented Plane wave + Local Orbitals Program for Calculating Crystal Properties" (K. Schwarz, TU Wien, Austria, 2001).
- <sup>37</sup>J. P. Perdew and Y. Wang, *Phys. Rev. B* **45**, 13244 (1992).